ICARUS 111, 489–502 (1994)

Radar Aperture Synthesis Observations of Asteroids

IMKE DE PATER

Astronomy Department, 601 Campbell Hall, University of California, Berkeley, California 94720

PATRICK PALMER

Department of Astronomy and Astrophysics, 5640 South Ellis, University of Chicago, Chicago, Illinois 60637

DAVID L. MITCHELL, STEVEN J. OSTRO, AND DONALD K. YEOMANS

Jet Propulsion Laboratory, California Institute of Technology, Pasadena, California 91109-8099

AND

LEWIS E. SNYDER

Department of Astronomy, 103 Astronomy Building, 1002 West Green Street, University of Illinois, Urbana, Illinois 61801

Received January 10, 1994; revised July 14, 1994

We report results of Goldstone-VLA, radar aperture-synthesis observations of the mainbelt asteroids 324 Bamberga and 7 Iris and the near-Earth asteroids 1991 EE and 4179 Toutatis. Simultaneous resolution of echoes in both angle and Doppler frequency provide new constraints on the mainbelt asteroids' pole directions: Bamberga's spin vector is within 40° of the south ecliptic pole, and the twofold ambiguity in Iris' pole direction (P. Magnusson, 1989, in *Asteroids II*, pp. 1180–1190) is resolved in favor of the ecliptic coordinates $\lambda = 15°$, $\beta = +25°$. For Bamberga, monostatic and bistatic radar echoes and VLA thermal-emission measurements, also reported here, are consistent with radiometric estimates of Bamberga's size and with the hypothesis that the asteroid is overlain by a regolith having a porosity of ~50%. Our near-Earth asteroid measurements required the development of new on-line VLA software that allows imaging of objects that are in the telescope's "near field." This software has been successfully tested on Toutatis at a distance of 0.06 AU and will be essential for VLA observations of Earth-approaching comets.

1. INTRODUCTION

In recent years radar has become a powerful tool in the study of asteroids (e.g., Ostro 1993). Although much of our knowledge of asteroids is based upon lightcurves, spectra, and infrared radiometry, radar observations can provide unique constraints on the geometric aspects of asteroids (shapes, sizes, and spin vectors) and on their surface properties (roughness, porosity, and metal abundance). If the signal to noise ratio (S/N) of the echo is sufficiently high, then the distribution of echo power in Doppler frequency and/or time delay can be used to image an object.

Aside from S/N requirements, which restrict the time delay and frequency resolutions, one limitation of delay-Doppler imaging involves an ambiguity in the locations of radar features. To remove this ambiguity and also to improve upon Goldstone's monostatic sensitivity, Muhleman and co-workers initiated bistatic radar experiments in which the Goldstone antenna transmits continuously at 3.5 cm and the VLA[1] receives the echo. Because the effective antenna area of the VLA is three times larger than that of the Goldstone antenna, the sensitivity of the "G-VLA" system can be up to three times that of a monostatic experiment at Goldstone. Muhleman and coworkers exploited the G-VLA system to detect echoes from various objects (Muhleman *et al.*, 1990, 1991, Butler *et al.* 1993, Slade *et al.* 1992). Another significant advantage of receiving the radar echo with the VLA is that the echo can be directly imaged at a number of different Doppler frequencies. The best instrumental frequency resolution of the VLA (381 Hz) is very coarse compared with resolutions obtainable with the Goldstone and Are-

[1] The VLA (Very Large Array) is part of the National Radio Astronomy Observatory, which is operated by Associated Universities, Inc., under a cooperative agreement with the National Science Foundation.

0019-1035/94 $6.00

cibo radar systems; however, provided that an echo can be resolved in frequency, direct imaging may allow the determination of an asteroid's sense of rotation and the position angle of its rotation axis in only a few hours of observing time.

Even if a target is unresolved in frequency, VLA observations can provide plane-of-sky positions in the coordinate frame of the VLA calibration sources with an accuracy of about 0.01 arcsec for point sources if S/N $\gtrsim$ 10. The combination of those measurements and line-of-sight delay/Doppler radar measurements can provide an extremely powerful data set for improving the ephemerides of near-Earth objects.

Here we report the first G-VLA radar observations of asteroids: A-array experiments on the mainbelt objects 7 Iris and 324 Bamberga and the near-Earth objects 1991 EE and 4179 Toutatis. We also discuss relevant results of monostatic Goldstone and Arecibo observations of those asteroids. Finally, to complement the radar observations of Bamberga, we report VLA 3.6-cm observations of the thermal emission from this asteroid. Our results provide new information about the asteroids' physical properties and demonstrate the G-VLA's potential for small-body remote sensing.

2. OBSERVATIONS

We used the G-VLA system to observe Iris, Bamberga, and 1991 EE in September 1991 and Toutatis in December 1992. A log of all the observations discussed is provided in Table I. The orbital motion of each asteroid was well known, even in the case of the near-Earth objects, since results from monostatic experiments conducted before the G-VLA observations were used in preparing the ephemerides. In each G-VLA experiment the frequency of Goldstone's continuous-wave (cw) transmission was continuously adjusted so that if the ephemeris were perfect and the asteroid were a point target, then the echo received by the VLA would be a spike at exactly 8510 MHz. (The bandwidth of the transmission was $\ll$0.001 Hz.) For each target the Doppler-prediction error for the asteroid's center of mass was known to be very small compared with the receiver's frequency resolution. Any observed frequency spreading of the echo around 8510 MHz can thus be attributed to Doppler broadening caused by the asteroid's rotation. During all G-VLA observations, the VLA was in its A configuration, with a maximum antenna separation of 36 km. The radar echoes were received by the VLA in a spectral-line mode in which 32 of 512 channels were recorded in one polarization (1 IF mode) with a frequency resolution of 381 Hz.

The signals transmitted from Goldstone were circularly polarized. Echo power generally occurs in both the opposite sense (OC) and the same sense (SC) of circular polarization as that of the transmitted signal. The sense of a circularly polarized signal is reversed upon reflection from a smooth surface, but SC echo power can arise from single backscattering from a rough surface, from multiple scattering, and from subsurface refraction effects. The circular polarization ratio (of SC to OC echo power) is thus a measure of the near-surface roughness at scales similar to the observing wavelength. Measured circular polarization ratios are less than 0.2 for most mainbelt asteroids (Ostro *et al.* 1985) and no greater than unity for near-Earth objects. Therefore, we configured the VLA to receive the OC echoes for our primary experiments on each target. For Toutatis we used four different transmit/receive polarization setups.

The radar power incident per unit projected area on the asteroid can be written

$$P_a = \frac{P_t G}{4\pi r^2}, \tag{1}$$

where P_t is the transmitter power, G is the elevation-dependent gain of the Goldstone antenna, and r is the distance to the object. The transmitter power is known to have been between 460 and 475 kW for all our observations. The nominal on-axis gain of the system was 2.6×10^7. The largest uncertainty in determining P_a results from errors in centering the target in the radar beam (pointing errors), which translate into variations in the effective antenna gain.

The equivalent isotropically scattered power is P_a multiplied by the radar cross section of the target, $\sigma = \hat{\sigma}\pi R^2$, where $\hat{\sigma}$ is the radar albedo and πR^2 is the target's projected area. The reflected signal is spread out in frequency by the asteroid's rotation and diluted by a factor of $1/(4\pi r^2)$ by the time it reaches the VLA. The echo flux is given by

$$\sum_i F_{\nu_i} \Delta\nu = \frac{P_t G \sigma}{(4\pi)^2 r^4}, \tag{2}$$

where $\Delta\nu$ is the single channel bandwidth, and F_{ν_i} is the flux density in a single channel. The primary VLA flux calibrators were 3C286 for the Iris observations and 3C48 for the Bamberga and Toutatis observations, with assumed flux densities of 5.24 and 3.27 Jy, respectively.[2] For an unpolarized calibrator, the power at each antenna in each of two orthogonal senses of circular polarization is $\frac{1}{2} S_c A_e$, where S_c is the total flux from the calibrator and A_e is the effective antenna area. A radar echo can have a high degree of net circular polarization, so to determine the echo flux in one sense of polarization alone (i.e.,

[2] 1 Jy = 10^{-26} Wm^{-2}Hz^{-1}

TABLE I
Observing Log

Target	Date (UT)	Time (UT)	RA (^{h} ^{m})	Dec (° ′)	D_{Earth} (AU)[a]	D_{Sun} (AU)[b]	Observing Mode[c]	Polarization trans/recv
	Sep. 5	04:14-04:55	23 07	+02 20	0.815	1.816	A-A	Dual[d]
	Sep. 6	04:13-04:54	23 06	+02 27	0.813	1.814	A-A	Dual
	Sep. 9	07:13-11:30	23 04	+02 46	0.807	1.809	G-VLA	RCP/LCP
	Sep. 13	08:03-10:43	23 00	+03 12	0.803	1.803	G-VLA	RCP/LCP
Bamberga	Sep. 14	08:19-09:54	22 58	+03 20	0.802	1.802	G-G	Dual
(1991)	Oct. 3	03:40-10:20	22 43	+04 54	0.831	1.780	Thermal	
	Oct. 8	03:20-07:05	22 41	+05 14	0.851	1.776	Thermal	
	Oct. 11	01:05-01:19	22 39	+05 26	0.863	1.775	A-A	Dual
	Oct. 12	01:10-01:24	22 39	+05 30	0.868	1.774	A-A	Dual
	Oct. 13	01:05-01:20	22 39	+05 34	0.873	1.774	A-A	Dual
	Sep. 15	03:44-11:20	22 42	+03 39	1.016	2.008	G-G	Dual
Iris	Sep. 16	03:07-06:04	22 42	+03 36	1.016	2.006	G-VLA	RCP/LCP
(1991)	Sep. 17	07:23-11:26	22 41	+03 27	1.016	2.004	G-G	Dual
	Sep. 28	03:07-09:45	22 33	+02 20	1.028	1.981	G-G	Dual
	Dec. 17	07:01-08:17	09 16	+10 56	0.063	1.023	G-VLA	RCP/LCP
Toutatis	"	08:17-08:36	"	"	"	"	"	RCP/RCP
(1992)	"	08:40-08:48	"	"	"	"	"	LCP/RCP
	"	08:48-08:57	"	"	"	"	"	LCP/LCP

[a] Earth–Target distance.
[b] Sun–Target distance.
[c] Transmit Station–Receive Station (A, Arecibo; G, Goldstone; VLA, Very Large Array). "Thermal" indicates a VLA thermal measurement.
[d] Here, dual polarization observing consists of transmitting an RCP signal and receiving both the LCP and RCP echoes.

in the 1-IF mode), one compares the measured power from the source with the measured power from the calibrator in that sense of polarization, or equivalently, one divides the total calibrator flux by two. The uncertainty associated with establishing the absolute flux density scale of the VLA is believed to be less than 3% (including both systematic and random errors). Deriving a target's radar cross section from the measured echo flux requires knowledge of P_a. Based upon the repeatability of monostatic radar observations, we attribute uncertainties of 30 and 20%, respectively, to monostatic and G-VLA radar cross section estimates.

In a separate experiment, Bamberga's thermal continuum emission was observed with the VLA in October 1991. Those observations were performed with a bandwidth of 100 MHz at a central frequency of 8440 MHz. By the time the continuum observations were performed, the array had moved to the more compact A/B configuration.

Radar and radio images were constructed from the interferometer data using the standard NRAO AIPS reduction package. Depending on the S/N of the data, we used either natural or uniform weighting. Natural weighting yields the highest sensitivity for weak, compact radio sources and was used to produce the radar images of Iris and Bamberga. The synthesized beam's full width at half power (FWHP) for these images is typically 0.26″. Bamberga's thermal emission and the radar images of Toutatis were mapped with uniform weighting, which provides the highest possible resolution at the expense of some sensitivity. The elliptical beam used for the Bamberga continuum imaging had a FWHP of 0.39″ × 0.29″ with the long axis at a position angle of 54°; for Toutatis the beam was approximately circular with a FWHP of 0.23″.

3. RESULTS

A. Bamberga

Bamberga is a C-class asteroid (Tholen 1989) with a visual geometric albedo of 0.057 ± 0.003 (Tedesco 1989)

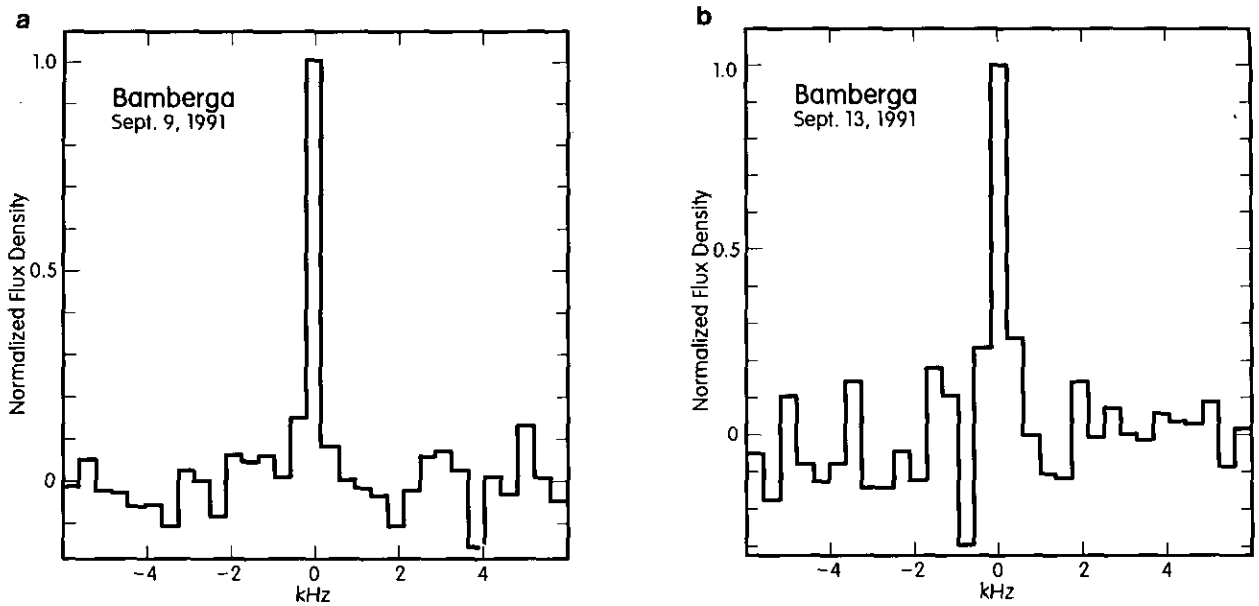

FIG. 1. G-VLA radar spectra of Bamberga on September 9 and 13, 1991, respectively. The peak flux density is normalized to unity.

and a rotation period of 29.43 hr (Scaltriti *et al.* 1980). Its "radiometric diameter" is 242 ± 7 km (Tedesco 1989), while occultation experiments yield a diameter of 228.2 ± 2 km (Millis and Dunham 1989). Those authors also conjecture that a "substantial chunk" of the object may be missing. Since the occultation data measure the object's size along only a few chords, while the infrared diameter likely represents an "overall average" size, we will use the latter to estimate Bamberga's radar albedo. No constraints on Bamberga's pole direction have been reported.

Radar spectra. Figure 1 shows the echo spectra obtained on September 9 and 13, 1991, with the G-VLA system. Most of the power is received in the central channel (16), with a small fraction in the two adjacent channels. During the same time period the asteroid was observed in monostatic radar experiments at Goldstone (λ = 3.5 cm) and Arecibo (λ = 12.6 cm) (Ostro *et al.*, in preparation). The monostatic echo spectra are displayed in Figs. 2 (a–c). The Arecibo spectra are quite skewed, suggesting an asymmetric shape.

For our purposes here, the instantaneous edge-to-edge echo bandwidth is

$$B(\phi) = \frac{4\pi\, D(\phi) \cos \delta}{\lambda P}, \qquad (3)$$

where ϕ is the rotation phase, P the synodic rotation period, δ the subradar latitude, λ the observing wavelength, and D the breadth of the asteroid's pole-on silhouette (Ostro *et al.* 1988). The perceivable bandwidth is often less than the edge-to-edge bandwidth given in Eq. (3) to an extent that depends on the radar scattering properties of the target and the S/N of the radar system. If $D(\phi)$, P, and δ are known (e.g., from optical and infrared observations), then the spectral shape of the echo constrains the radar scattering properties of the target. For example, OC echoes from smooth surface elements are always dominated by specular reflections from elements that are tilted in the direction of the radar. For nearly spherical objects, such as the Moon and Mercury, such regions are concentrated near the center of the projected disk, where Doppler shifts caused by the object's rotation are relatively small. Diffuse echo power (SC and OC) is much less centrally concentrated and weaker. Consequently, OC echoes from such objects consist of a "specular spike" at small Doppler shifts and relatively weak wings. In contrast, none of the mainbelt asteroids that have been observed by radar exhibits such a strongly peaked OC echo, despite the fact that the circular polarization ratios of these objects are generally small.

Our spectra in Figs. 1 and 2 place lower bounds on the observed echo bandwidth for Bamberga ($B \gtrsim 195$ Hz at 12.6 cm and $B \gtrsim 720$ Hz at 3.5 cm) that imply $D_{max} \cos \delta \gtrsim 210$ km, where D_{max} is the maximum breadth of Bamberga's pole-on silhouette. Given the available optical/IR constraints on size, we conclude that δ must have been within 30° of zero.

G-VLA images. Figure 3a shows a Bamberga image from the sum of the echoes obtained in all frequency channels on September 9 and 13. Since the data were taken on different days, the echo flux on September 13

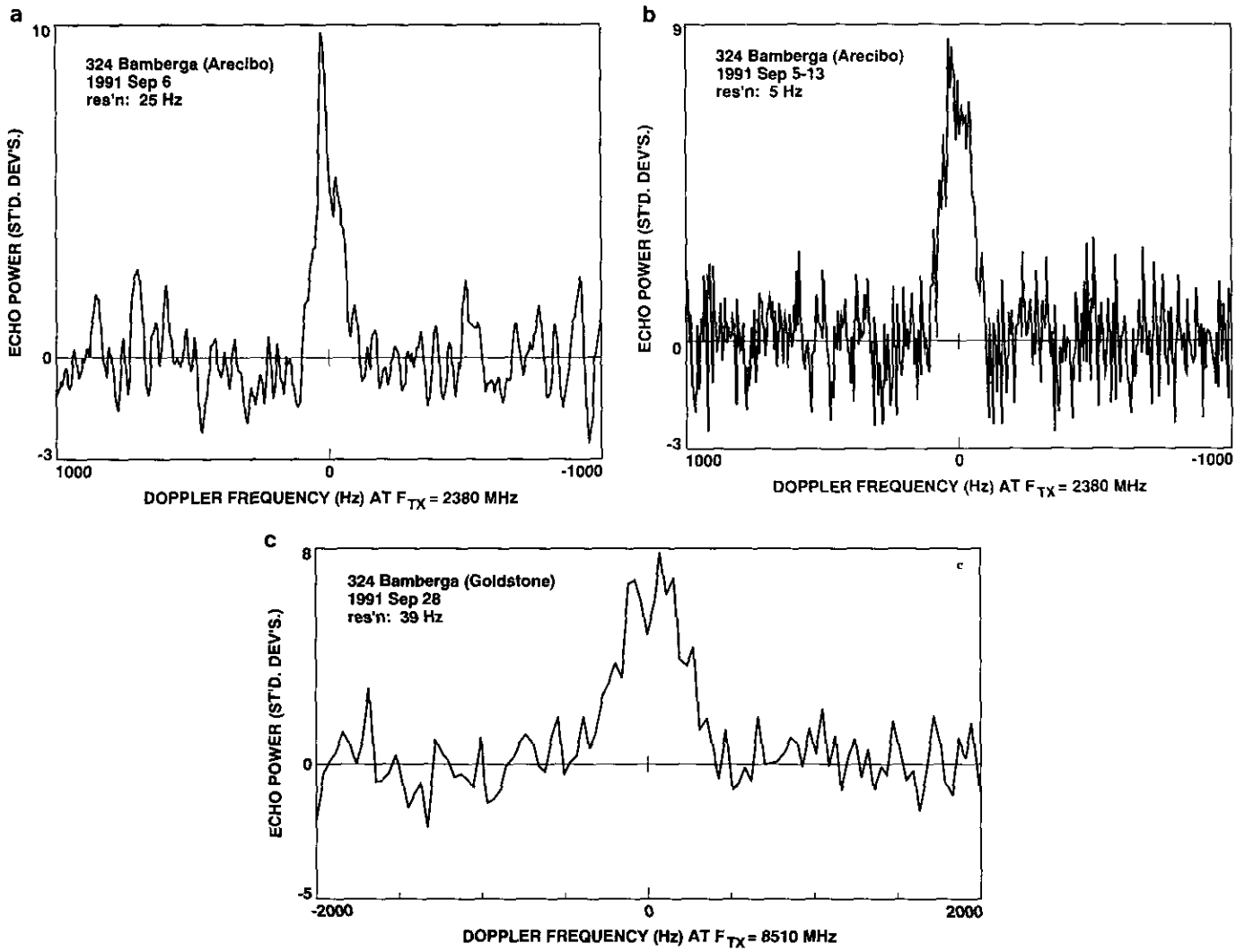

FIG. 2. Monostatic, OC echo spectra obtained for Bamberga (a) from a single Arecibo run on Sep. 6, (b) from a weighted sum of Arecibo spectra obtained during Sep. 5–13, and (c) from Goldstone observations on Sep. 28. Echo power, in standard deviations, is plotted vs the Doppler frequency (relative to that predicted for hypothetical echoes from the asteroid's center of mass) at the indicated transmitter frequency, F_{TX}. The spectra are from Ostro *et al.* (in preparation).

has been scaled to correct for the changing geometric dilutions of the transmitted and received signals. In addition, the interferometer *UV*-spacings have been scaled so that the asteroid's angular size appears constant while its distance changes. Figures 3b and 3c show images on September 9 and 13, respectively, in the individual channels. The solid line shows the image of the center channel, 16, and superimposed are contours of the neighboring channels: 15 (redshifted frequency) with dashed lines and 17 (blueshifted frequency) with dot–dashed lines.

The images obtained in channels 15 and 17 are displaced from that for the center frequency: channel 16 is centered on the projected rotation axis, while channels 15 and 17 represent regions of the asteroid on opposite sides of the rotation axis. The east side of the asteroid is receding, while the west side is approaching—that is, the rotation is *retrograde*. Figure 4 shows the positions of the peak intensities in each channel as estimated from Gaussian fits. The position angle of the normal to the line connecting channels 15 and 17 provides a reasonable estimate of the position angle (PA) of the rotation axis projected onto the sky; we measure PA = 155° ± 10°.

Together, our estimates of the subradar latitude and of the position angle of the projected rotation axis constrain Bamberga's pole to be within the shaded area centered on the filled circle at ecliptic coordinates of $\lambda = 2°$ and $\beta = -81°$ in Fig. 5. The uncertainty region was determined by mapping the error bars from the radar aspect angle and the G-VLA position angle onto the sky.

Radar reflectivity. The total radar echo flux density

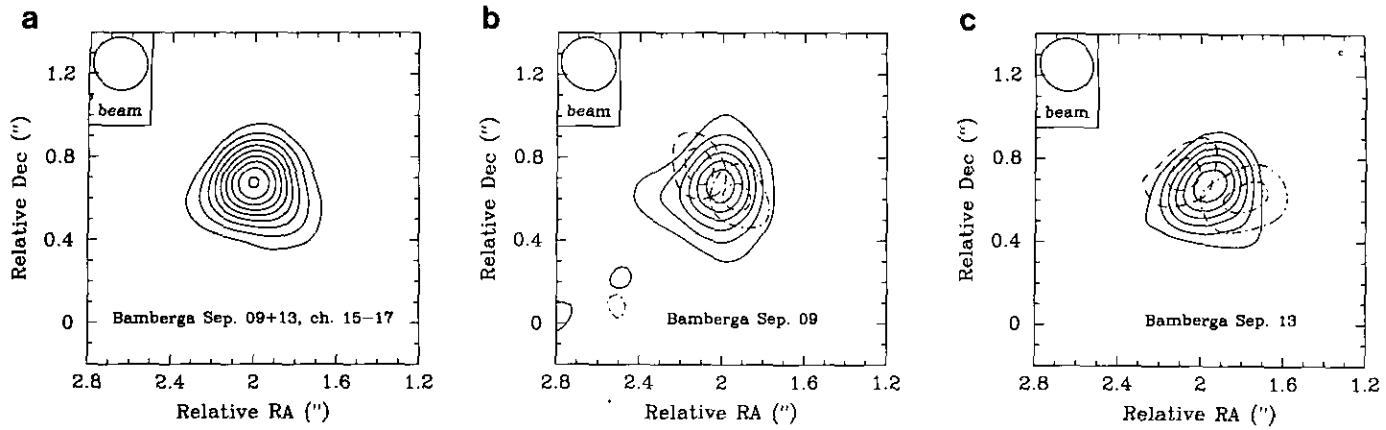

FIG. 3. G-VLA radar images of Bamberga. (a) The total flux density from September 9 and 13, summed over the three center channels (15–17). Contour levels are from 3 to 19 *SD* (standard deviations) in steps of 2 *SD*, with 1 *SD* = 6 mJy/beam. (b) Radar echoes on September 9 in channels 15 (dashed contours, redshifted), 16 (solid contours), and 17 (dot–dashed contours, blueshifted). Contour levels are from 3 to 13 *SD* in steps of 2 *SD*, with 1 *SD* = 3.9 mJy/beam. (c) Same as (b) for September 13 with 1 *SD* = 5.5 mJy/beam. Right ascension and declination are plotted relative to ephemeris predictions based on an orbit estimated from pre- 1988 astrometry.

from Bamberga can be related to the radar cross section σ (km^2) and albedo $\hat{\sigma}$ via Eq. (2),

$$\sum_i F_{v_i} = (9.4 \times 10^{-5})\sigma = (4.34 \pm 0.25)\hat{\sigma} \text{ Jy}, \qquad (4)$$

where we have summed over all channels. We assumed an effective disk diameter of 242 ± 7 km in the conversion from σ to $\hat{\sigma}$. The total flux density as determined from Fig. 3a, F_r = 225 ± 15 mJy, yields estimates of the radar cross section, σ = 2400 ± 480 km^2, and the radar albedo, $\hat{\sigma}$ = 0.05 ± 0.01.

Estimates of the radar cross section from monostatic radar data obtained at Arecibo and Goldstone fall within 25% of 3000 km^2, corresponding to a radar albedo $\hat{\sigma}$ = 0.07 ± 0.02, which is consistent with the G-VLA number. Bamberga's radar albedo apparently is between the lunar value (~0.07) and the value for the C-class mainbelt asteroid Ceres (0.05; Ostro *et al.* 1985).

The OC radar albedo can be expressed (Ostro *et al.* 1991) as the product of the Fresnel power reflection coefficient at normal incidence, R_o, and the radar backscatter gain, g:

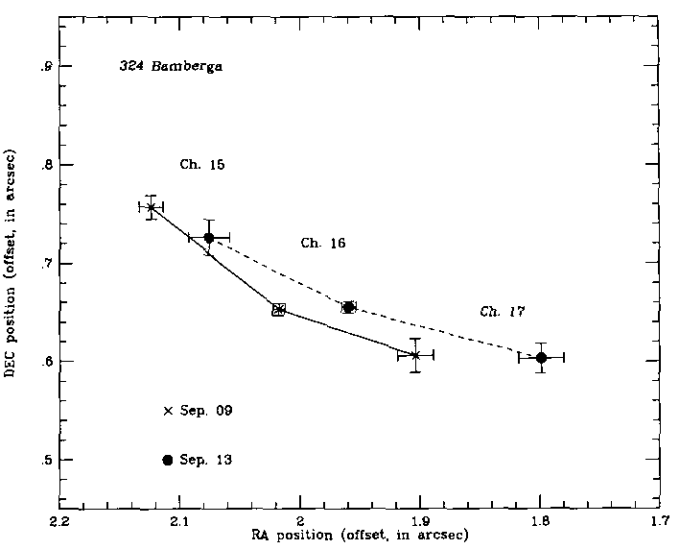

FIG. 4. The position of Bamberga's peak echo intensity in each VLA frequency channel. The positions are measured in arcseconds from the image center.

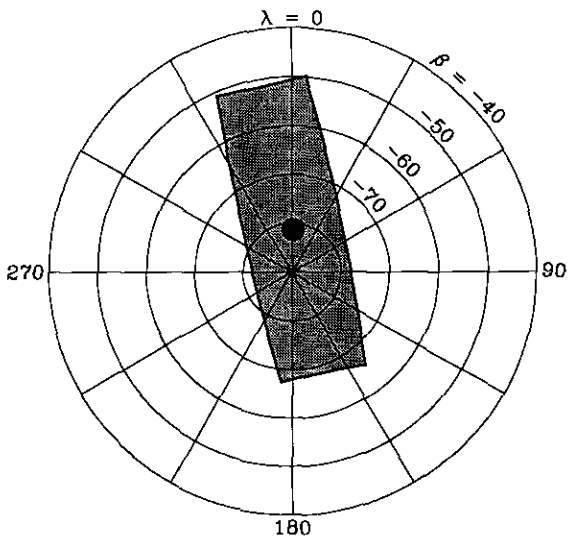

FIG. 5. Combined bistatic and monostatic radar data constrain Bamberga's spin vector to be within the shaded region centered on the filled circle. An ecliptic coordinate system is shown centered on the south pole with latitudes $\beta \leq -40°$.

$$\hat{\sigma} = gR_0. \tag{5}$$

This gain depends on the target's angular scattering law, shape, and orientation; it is unity for a smooth sphere and is somewhat larger when wavelength-scale scatterers and/or surface topography are present. The Fresnel power reflection coefficient R_0 is related to the complex dielectric constant ε of the surface:

$$R_0 = \left(\frac{1-\sqrt{\varepsilon}}{1+\sqrt{\varepsilon}}\right)^2. \tag{6}$$

It has been shown empirically that the densities and the complex dielectric constants of most lunar and terrestrial powders (ρ_p and ε_p) can be related to those of the parent rocks (ρ_s and ε_s) via the Rayleigh mixing formula (Campbell and Ulrichs 1969):

$$\frac{1}{\rho_p}\left(\frac{\varepsilon_p - 1}{\varepsilon_p + 1}\right) = \frac{1}{\rho_s}\left(\frac{\varepsilon_s - 1}{\varepsilon_s + 1}\right). \tag{7}$$

Ostro *et al.* (1991) show a graphical representation of the radar reflectivities of solid and powdered meteoritic materials of various compositions and densities.

Since g is at least unity, Bamberga's G-VLA radar albedo, $\hat{\sigma} = 0.05 \pm 0.01$, constrains the complex dielectric constant: $|\varepsilon| \leq 2.7$. We are therefore probing regolith rather than rock. This is consistent with collisional theories that predict most asteroids with sizes over 100 km to be overlain by a thick (10- to 500-m), fine-grained regolith (McKay *et al.* 1989). If Bamberga, a C-type asteroid, consists of carbonaceous chondritic material, the observed radar reflectivity implies a regolith porosity of ~50% (Eq. (7); see Ostro *et al.* 1991).

Thermal emission. Bamberga's thermal radio emission was observed on October 3 and 8. Since part of the array had moved to a more compact configuration, the resolution is lower than during the G-VLA radar observations. The thermal image (Fig. 6) was constructed with the uniform weight option, resulting in an elliptical beam with FWHP of 0.39″ and 0.29″ at a position angle PA = 54°. We wish to compare G-VLA radar results with VLA thermal measurements obtained nearly 1 month later. Therefore, we have adjusted the angular and flux scales in Fig. 6 to compensate for the asteroid's greater distance in October. The apparent elongation of the image is caused by the elliptical Gaussian beam. No departure from a uniform disk with a diameter of ~242 km can be detected.

The observed thermal flux density can be converted into a disk-averaged brightness temperature with the Rayleigh–Jeans' approximation to Planck's law,

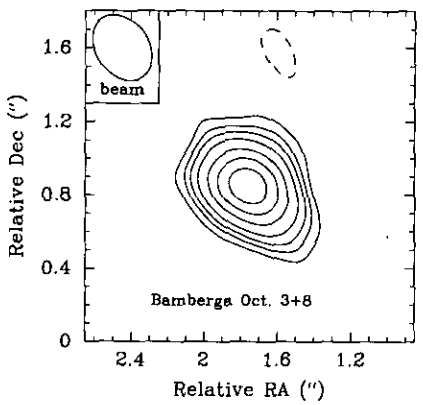

FIG. 6. Bamberga's thermal radio emission at 3.6 cm. Contour levels are 3, 5, 7, 10, 15, 20, and 25 *SD*, with 1 *SD* = 25.6 μJy/beam. The dashed contour is at −3*SD*.

$$T_b = \frac{490\lambda^2 S}{R^2}. \tag{8}$$

where λ is the observing wavelength (3.53 cm) and R is the apparent radius in arcseconds (0.206″). The flux density determined from a naturally weighted image, $S = 1.31 \pm 0.04$ mJy, yields a disk-averaged brightness temperature of $T_b = 188 \pm 22$ K, where the uncertainty is dominated by the 7 km uncertainty in the disk diameter. Our measured brightness temperature agrees with the value of 202 ± 54 K (scaled to a 242 km disk diameter) that was obtained at a wavelength of 2 cm by Dickel (1979).

Thermal models. We calculated the thermal microwave brightness temperature for two models of Bamberga's surface by adapting a thermophysical model initially developed for Mercury (Mitchell 1993, Mitchell and de Pater 1994). Approximating the asteroid as a smooth, nonscattering sphere ($g = 1$) with Bamberga's orbital and rotational parameters, we considered two extreme models: a rocky surface and one covered by a thick, homogeneous, fine-grained regolith. The asteroid's surface is assumed to have thermal and electrical properties similar to either lunar rocks or the lunar regolith. Parameters of the two models are given in Table II.

The opacity of the surface to microwaves is expressed in terms of the one-way electrical skin depth, L_e,

$$L_e = \frac{\lambda}{2\pi\sqrt{\varepsilon_r}\tan\Delta}, \tag{9}$$

where λ is the observing wavelength, ε_r is the real part of the dielectric constant, and tan Δ is the loss tangent, which is the ratio of the imaginary part of the dielectric constant to the real part. Lunar rocks typically have a complex dielectric constant of 7–0.2i at a wavelength of

TABLE II
Asteroid Models

Parameter	Rocky Surface	Dusty Surface
visual albedo	0.057	0.057
infrared emissivity	0.9	0.9
rotation period	1.226 days	1.226 days
density	3.0 g cm^{-3}	1.5 g cm^{-3}
thermal conductivity	10^5 erg cm^{-1} s^{-1} K^{-1}	10^3 erg cm^{-1} s^{-1} K^{-1}
observing wavelength	3.53 cm	3.53 cm
dielectric constant	7.0	2.5
loss tangent	0.030	0.010

3.5 cm (Gary and Keihm 1978), which yields L_e(rock) = 7 cm. Provided that tan $\Delta \ll 1$, a regolith density of 1.5 g cm^{-3} is required to provide a dielectric constant of 2.5 that is consistent with the G-VLA radar albedo and $g = 1$. Lunar dust at this density would have a loss tangent of 0.01, which yields L_e(dust) = 35 cm. The thickness of the regolith is assumed to be several times larger than L_e(dust).

Figure 7 shows diurnal temperature variations in the surface layers of the two models. The thermal conductivity of rock is large, so these variations have a small amplitude and penetrate to a depth of about 50 cm, which is much larger than the electrical skin depth of 7 cm (Fig. 7a). In contrast, the thermal conductivity of dust is much lower, so diurnal temperature variations have a large amplitude and are confined to the upper ~10 cm, which is much smaller than the electrical skin depth of 35 cm (Fig. 7b). Consequently, the brightness temperature in either model is only weakly influenced by diurnal effects and is thus not very sensitive to our assumptions about the thermal and electrical properties of the surface. For example, changing the loss tangent by a factor of two in either model causes variations in the disk-averaged brightness temperature of only ~1 K.

A significant difference between the rock and dust models occurs in the microwave emissivity. If we ignore scattering, the normal emissivity is 0.80 for the rocky surface and 0.95 for the optically thick dust layer. The latter value is complementary to the G-VLA OC radar albedo ($\hat{\sigma}$ = 0.05), since the reflectivity and emissivity of a smooth, nonscattering sphere are complementary under the same viewing conditions. If scattering is present, the sum of the reflectivity and emissivity remains unity when averaged over 2π steradians (conservation of energy) but not necessarily when viewed from a specific angle. Tryka and Muhleman (1992) show that for strict backscatter, as in a radar experiment, this sum is only slightly less than unity. Thus, the complement of the radar albedo provides a reasonably unbiased estimate of the normal emissivity of a smooth sphere.

In order to calculate the disk-averaged brightness temperature, the emissivity at nonnormal angles of incidence is determined from the Fresnel formulas assuming a smooth, spherical surface ($g = 1$). The disk-averaged brightness temperature for a rocky Bamberga, with its rotational axis perpendicular to the line of sight ($\delta = 0°$), is 166 K. The brightness temperature is only somewhat higher, 177 K, for a dusty Bamberga because the higher emissivity is partly offset by the greater transparency of

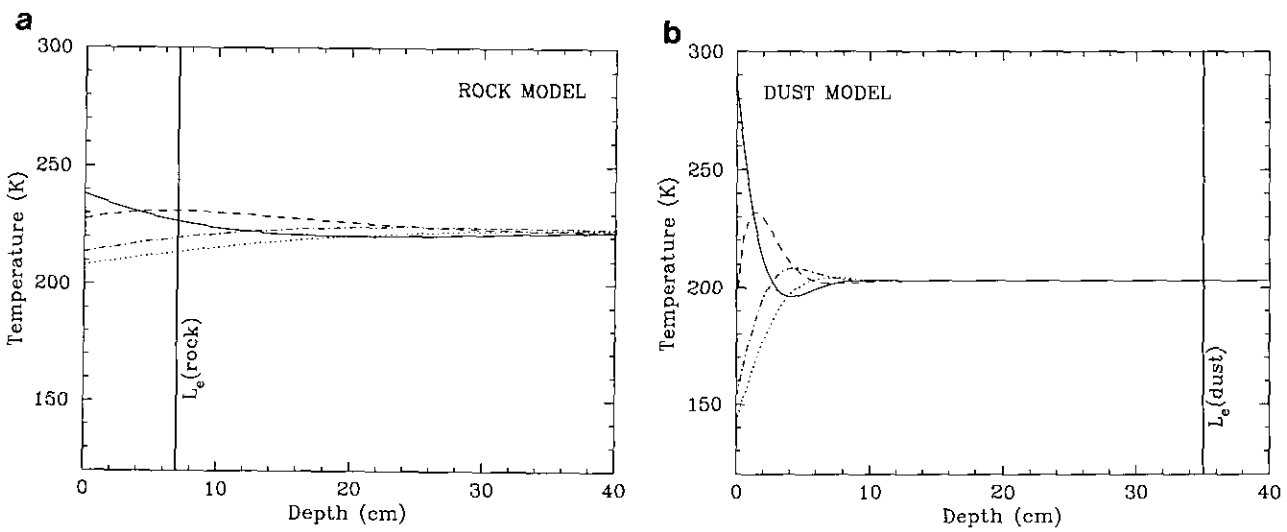

FIG. 7. Equatorial temperature profiles within the surface layers of two spherical asteroid models: (a) rocky surface, (b) surface covered by a thick regolith. Temperature profiles are shown for local noon (solid curve), sunset (dashed curve), midnight (dot–dashed curve), and sunrise (dotted curve). The electrical skin depths (L_e) are shown by bold vertical lines.

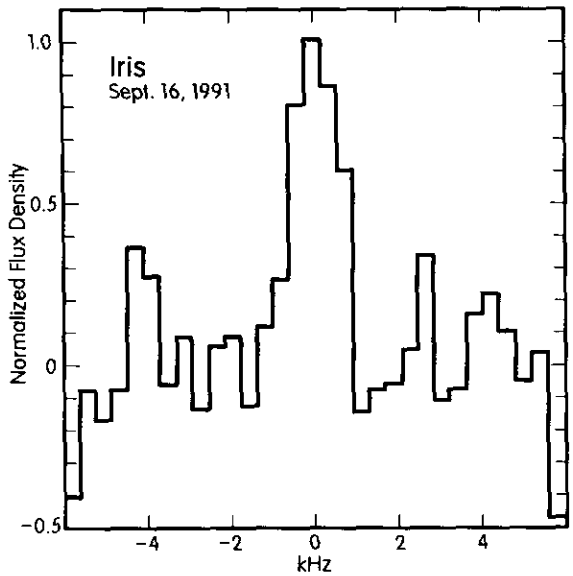

FIG. 8. Radar spectrum of 7 Iris, obtained in the G-VLA experiment on Sep. 16, 1991. The flux density along the vertical axis is normalized to the peak intensity in the spectrum.

the warm surface layers. When the pole is tilted toward the Sun, the asteroid appears brighter because the visible polar region is always in sunlight and is therefore warmer. If $|\delta| = 30°$, the brightness temperatures of the rocky and dusty asteroids increase to 173 K and 189 K, respectively. Roughness at size scales much larger than the observing wavelength also results in $g > 1$ (Ostro *et al.* 1985). If this is the case for Bamberga, then the above thermal calculations, which assume $g = 1$, underestimate the disk-averaged brightness temperature. Therefore, on the basis of the thermal data alone, we cannot discriminate between a rocky and a dusty surface, nor can we further constrain the pole direction; however, the data are consistent with a 242-km-sized object covered by a thick regolith.

B. Iris

Iris is an S-class asteroid (Tholen 1989) with a visual geometric albedo $A = 0.21 \pm 0.01$ and a radiometric diameter of $D = 203 \pm 5$ km (Tedesco 1989). The asteroid rotates in a prograde sense with a period of 7.139 hr (Magnusson 1989, and references therein). Visual lightcurves provide two possible sets of ecliptic coordinates for the rotational pole (Magnusson 1986): $\lambda = 15 \pm 5°$ and $\beta = +25 \pm 15°$ (P1 solution), or $\lambda = 195 \pm 5°$ and $\beta = +15 \pm 15°$ (P2 solution). Either result translates into a subradar latitude δ with an absolute value between 35° and 65° during our observations. Visual lightcurves of the asteroid show maximum variations of 0.25 magnitudes, which have been attributed primarily to variations in the projected surface area of the asteroid as it rotates. To account for the observed lightcurves, the asteroid's shape has been approximated by a triaxial ellipsoid with $a/b \simeq b/c \simeq 1.2$ to 1.4, where rotation is about the c-axis (Magnusson 1989, and references therein). Since the geometry and surface composition of Iris have been studied by several other techniques, the asteroid served as a good test object for our bistatic radar observations.

Spectra. Echo spectra were obtained at the VLA on September 16, 1991 (Fig. 8), and monostatically at Goldstone on September 15, 17, and 28 (Fig. 9). If Iris were a sphere with a diameter within 5 km of 203 km, and if the available constraints on pole direction were valid, then the bandwidth would be within 270 Hz of 1610 Hz (see Eq. (3)). The elongation of Iris' shape suggested by the amplitude variations in its visible lightcurves are expected to cause variations on the order of 10% in the bandwidth. The perceptibility of such variations would depend on the asteroid's radar scattering law and on the S/N, which for our observations is not very high. Still, our spectra seem consistent with expectations for Iris' bandwidth.

G-VLA images. Figure 10 shows (a) an average of channels 15–18, (b) an image of channel 16 alone, and (c) a comparison of channels 15 (dashed line) and 17 (solid line). The S/N in channel 18 was insufficient to provide a reliable image.

The images obtained in channels 15 and 17 do not coin-

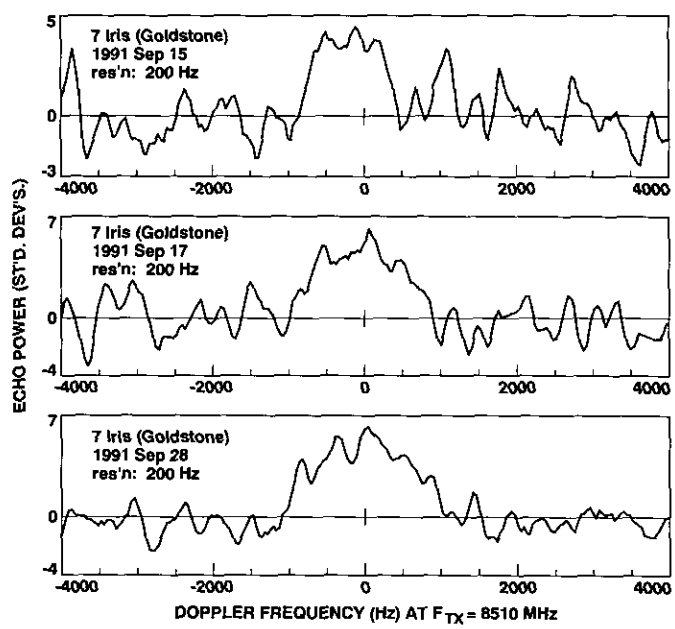

FIG. 9. Goldstone monostatic, OC echo spectra obtained for Iris on Sep. 15, 17, and 28. Echo power, in standard deviations, is plotted vs the Doppler frequency (relative to that predicted for hypothetical echoes from the asteroid's center of mass) at a transmitter frequency of 8510 MHz.

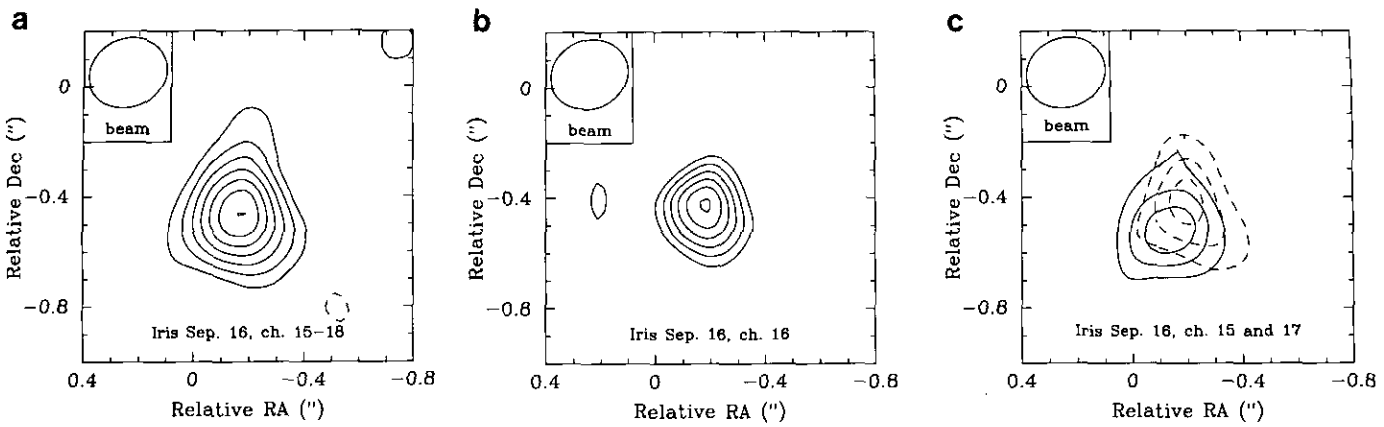

FIG. 10. G-VLA radar images of Iris. (a) Image of the radar echo summed over the four center channels (15–18). Contour levels are from 3 to 15 *SD* in steps of 2 *SD*, with 1 *SD* = 10 mJy/beam. The dashed contour is at − 3 *SD*. (b) Image of the radar return signal in the center channel (16). Contour levels are from 3 to 8 *SD*, with 1 *SD* = 5.3 mJy/beam. (c) Images of the signals received in channels 15 (redshifted channel; dashed line) and 17 (blueshifted channel; solid line). Contour levels are as in (a), with 1 *SD* = 5.3 mJy/beam. Right ascension and declination are plotted relative to ephemeris predictions based on an orbit estimated from pre-1988 astrometry.

cide. The approaching (blueshifted) side of Iris is observed in channel 17, while the receding (redshifted) side is observed in channel 15. This confirms the prograde sense of rotation for Iris. Figure 11 shows the positions of the peak intensities in each channel, and also plots the position angles of the projected spin vectors corresponding to Magnusson's (1986) two pole solutions. The spin vectors are drawn to radiate from the midpoint of the line connecting the centroids of channels 15 and 17. Since Magnusson's P1 pole solution is nearly orthogonal in the plane of the sky to the P2 solution, our results remove the pole ambiguity in favor of the P1 solution.

Radar reflectivity. The radar cross section and radar albedo of an object are related by Eq. (2). For Iris we find

$$\sum_i F_{v_i} = (3.75 \times 10^{-5})\sigma = (1.22 \pm 0.05)\hat{\sigma}\ \text{Jy}, \quad (10)$$

where we have assumed an effective disk diameter of 203 ± 5 km. The total observed flux density has been determined from Fig. 10a: $F_r = 220 \pm 20$ mJy. This corresponds to a radar cross section $\sigma = 6000 \pm 1200$ km^2 and a radar albedo $\hat{\sigma} = 0.18 \pm 0.04$.

Monostatic radar data obtained at Goldstone during September 1991[3] yield a radar cross section of 5000 ± 1500 km^2, which correspond to a radar albedo of 0.15 ± 0.05. This value agrees well with that determined by the G-VLA experiment and the value of 5900 km^2, measured at Arecibo in December 1980 (Ostro *et al.* 1985), when Iris' subradar latitude was within 20° of its value during our 1991 observations.

C. Toutatis

In data reduction packages for interferometric radio astronomy, incoming wave fronts are assumed to be plane waves. This approximation usually holds because radio sources are effectively infinitely distant. However, when

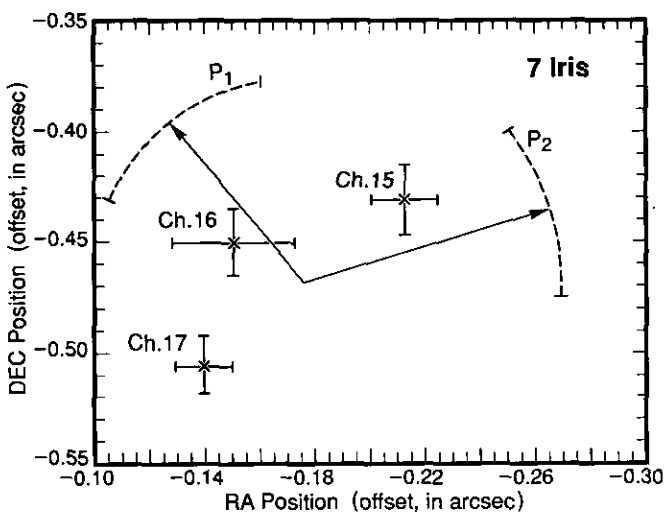

FIG. 11. The position of Iris' peak echo intensity in each VLA frequency channel. The positions are measured in arcseconds from the image center. The two arrows with dashed arcs indicate the projections of the two pole solutions, P_1 and P_2, from Magnusson (1986) with their uncertainties.

[3] The radar cross section on September 15 was a factor of 2 smaller than the other values, which we attributed to an unknown problem (pointing errors?) and ignored in the analysis.

the VLA is in its most extended (A) configuration, the plane wave approximation no longer holds for objects in the inner Solar System. The error depends on the distance along the line of sight between the actual spherical wave front and an idealized plane wave front that coincides with it at the center of the array. This distance increases quadratically away from the center of the array. For objects near 0.06 AU, the distance amounts to a full wavelength at the longest baselines. The actual wave will arrive later than the assumed plane wave and a phase error results. The phase error is different for each baseline and varies with time as the Earth rotates and the object moves along its orbit.

Bistatic G-VLA observations of the near-Earth asteroid 1991 EE were performed *without* near-field phase corrections on September 9 and 13 1991, when the object was at a geocentric distance of ~0.06 AU. The resulting phase errors were so large that it was impossible to construct images from the data. The asteroid was detected only in the autocorrelation mode of the VLA, which ignores phase information and is thus analogous to a total power measurement by a single dish. Motivated by this experience, K. Sowinski and P. Palmer developed on-line software to perform the near-field correction.

An important test of this new software was a bistatic G-VLA observation of Toutatis on December 17, 1992, when the asteroid was at a geocentric distance of ~0.06 AU. Because of the object's proximity, the radar echo was so strong that it was easily detected in a single 10-sec integration. The amplitude of the signal was essentially constant as a function of baseline length, which is the expected signature of an unresolved source at infinity. Toutatis could only have appeared this way if the near-field corrections were properly applied.

To check the polarization circularity of the Goldstone transmissions, we observed Toutatis in all four possible transmit/receive combinations of right and left circular polarization. No instrumental ellipticity of polarization was detected (see below). Since most data were taken with Goldstone transmitting RCP and the VLA receiving LCP, the data quality is highest for this setup. Since Toutatis' echo bandwidth was about 2.2 Hz (Ostro *et al.* 1993), the echo was received only in the center channel.

Each Toutatis scan was approximately 4–5 min long. The high S/N allowed us to make separate images of each scan. The asteroid was not located at the center of the field and displayed a linear motion throughout the observing run. Total displacements of ~1.2″ in right ascension and ~1.4″ in declination were recorded, and were later traced to an error in generating the positions of date from the ephemeris. Angular rates of motion determined from differences in B1950 coordinates had been applied to positions of date. The maximum possible error caused thereby was $\sim 10^{-3} \times$ the angular rate of motion (per day) of the object. This error was insignificant for Iris and Bamberga, but was important for Toutatis, which was moving >8000″ per day at the time of these observations. We compensated for this error by making phase adjustments to all baselines at all times so that the asteroid always appeared in the center of the field.

All "corrected" *UV*-data were combined and Fourier transformed for each polarization set-up. Our highest quality data set (RCP/LCP setup) could be self-calibrated (e.g., Cornwell and Fomalont 1989), which further improved the image (Fig. 12a). The resolution (FWHP) is 0.24″ × 0.22″ (~10 km at the source) at a position angle PA = −14°. Any elongation can be revealed by subtracting from the center of the image a point source model with a flux density equal to the peak flux of the observed source. The resulting difference image (Fig. 12b) indicates that Toutatis is elongated along the direction of the two residual features at PA ≃ −61°. This elongation cannot result from slight errors that might remain in the above-mentioned differential ephemeris corrections, since these would cause an apparent elongation along a direction with PA ~ +60°. Although Toutatis is certainly elongated along PA ≃ −61°, the separation between the two residual features, ~15–16 km, is determined primarily by the beam size. We derive an upper limit of 30 km for the asteroid's extent along this direction. This number is much larger than Toutatis' size as estimated from the monostatic radar data (Ostro *et al.* 1993).

Total flux densities. We determined the flux densities for each of the four images. The flux densities of the two OC images were equal to within the uncertainties (ignoring internal and absolute calibration errors): $F_{oc} = 3.13 \pm 0.01$ Jy. The flux densities in the two SC images were also equal to within the uncertainties: $F_{sc} = 1.21 \pm 0.015$ Jy. The corresponding radar cross sections are: $\sigma_{oc} = 1.24 \pm 0.25$ km^2 and $\sigma_{sc} = 0.48 \pm 0.1$ km^2, where we have adopted a ~20% total uncertainty. Our estimate of the circular polarization ratio is $\mu_c = F_{sc}/F_{oc} = 0.38 \pm 0.01$. In the latter estimate we have ignored the systematic ~20% uncertainties, which are probably the same in the SC and OC cross section estimates. These results will be discussed elsewhere, in the context of the monostatic radar results (Ostro *et al.*, in preparation).

4. ASTROMETRIC POTENTIAL OF G-VLA OBSERVATIONS

As mentioned earlier, G-VLA angular positions are potentially useful for refining orbits of closely approaching objects. However, to make use of these positions to improve an asteroid's ephemeris, one must know the relationship of the VLA calibrator frame to the VLBI radio frame, the optical FK5 frame, and the dynamical frame

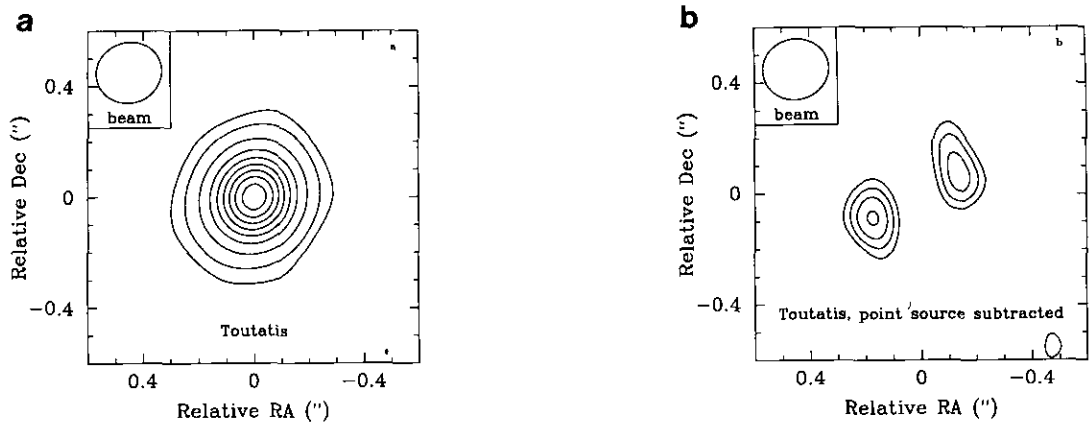

FIG. 12. G-VLA radar images of Toutatis. (a) Radar image with a resolution of 0.24" × 0.22". Goldstone transmitted RCP, and the VLA received LCP. Contour levels are: 3, 10, 30, 60, 90, 120, 150, 180, and 210 *SD*, with 1 *SD* = 13 mJy/beam. (b) Radar image of Toutatis after a point source of 3 Jy was subtracted from the center of the image. Contour values are: 3, 4, 5, and 6 *SD*, with 1 *SD* = 12.5 mJy/beam.

of the planetary ephemerides. The VLA calibrator frame and the VLBI frame are expected to agree with an accuracy set by the sizes of the VLBI sources (a few milliarcseconds). Most asteroid position measurements are made optically and are ultimately tied to the FK5 system. At present, the three reference frames are believed to be tied together with an accuracy of approximately 0.02 arcsec (Fomalont 1993). While this situation is expected to improve by an order of magnitude in the next decade, the present accuracy of the reference frame ties is probably the limiting factor in the use of VLA asteroid positions.

Figure 13 shows the results of an error analysis designed to quantify how G-VLA angular measurements can complement optical astrometry. The semimajor axis of the plane-of-sky position error ellipse for 4179 Toutatis is plotted as a function of time between 1995 and 2005 for three different cases. In the first case (denoted "O" in the figure), only the existing optical astrometric data from 1934 to February 1993 were analyzed using the error covariance technique of Yeomans *et al.* (1987). Each of the 316 optical measurements was assigned an uncertainty of 1 arcsec. Note that Toutatis' position error ellipse is smallest during the asteroid's close approaches to Earth in late 1996, 2000, and 2004. In the second case (denoted "R"), preliminary delay and Doppler radar measurements taken at Goldstone and Arecibo in 1992 from Nov. 27 to Dec. 18 (Ostro *et al.* 1993), were included with the optical data. We assigned conservative noise estimates of 10 μsec to each of the 34 delay measurements and 1 Hz to each of the 21 Doppler measurements. In the final case (denoted "V"), we included six hypothetical plane-of-sky VLA measurements with the actual optical and radar data. Pairs of VLA measurements were assumed to have taken place 2 days before, the day of, and 2 days after the asteroid's close approach to Earth on December 8, 1992. All six VLA observations were assigned an uncertainty of 0.02 arcsec. The combined VLA and radar observations reduce the asteroid's future position uncertainty by as much as a factor of four relative to optical observations alone.

5. POTENTIAL OF G-VLA COMET OBSERVATIONS

We believe that the greatest potential of small body radar aperture synthesis is in high-resolution imaging of

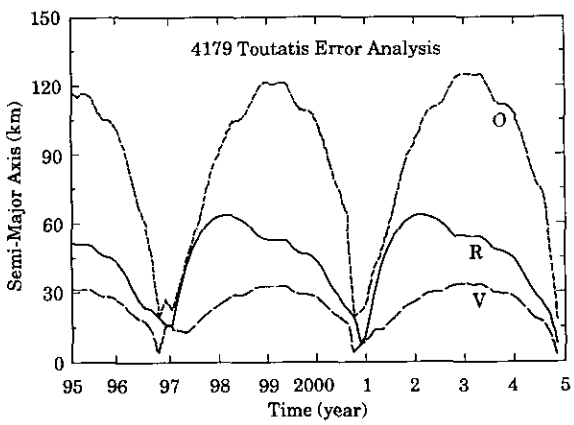

FIG. 13. Improvements in the ephemeris of 4179 Toutatis when both line-of-sight radar and plane-of-sky VLA measurements are included in the orbital analysis. The semimajor axis of Toutatis' position error ellipse is plotted as a function of time from 1995 to 2005. Curve O includes only optical data from 1934 to February 1993. In curve R, radar delay and Doppler measurements taken between Nov. 27 and Dec. 18, 1992, are added; curve V includes, in addition, six hypothetical VLA position measurements which were assumed to have taken place on Dec. 6, 8, and 10, 1992 (around closest approach).

cometary comas. Monostatic radar observations of comet IRAS–Araki–Alcock (IAA) in 1983 suggested the presence of a 1000-km cloud of centimeter-sized particles whose total radar cross section was one-third of the nuclear cross section (Harmon *et al.* 1989, Goldstein *et al.* 1984). For Comet Halley in 1985, echoes from a large-particle cloud obscured those from the nucleus (Campbell *et al.* 1989). Plane-of-sky resolution of the echoes from such swarms would constrain the cloud geometry, particle dynamics, and ejection phenomena in ways impossible with Doppler-only or delay-Doppler radar experiments. (Comet IAA came within 0.03 AU from Earth, and observations of IAA with the current G-VLA radar could have yielded images placing up to a few hundred resolution elements on the cloud. Even for Halley at 0.42 AU, G-VLA images could have directly revealed the cloud's dimensions.) At close proximity, however, a comet's angular rate of motion can exceed that of 1991 EE and Toutatis during our observations. The experiments described in this paper provided crucial tests for A-array radar observations of close, rapidly moving targets, and we feel that the G-VLA system is now ready to take advantage of future opportunities to image closely approaching comets. The next known opportunity for G-VLA imaging of a cometary coma is in 2006, when Schwassmann–Wachmann 3 passes 0.09 AU from Earth. Discovery of a new, closely-approaching comet would offer a more immediate opportunity.

ACKNOWLEDGMENTS

We thank K. Sowinski for his help with the VLA software for near-Earth objects. In addition, discussions with C. Wade, E. Fomalont, and G. Kaplan are highly appreciated. This work was funded in part by NASA Grant NAGW-1131 to the University of Illinois. Much of this research has been carried out while IdP was a Miller Research Professor in the Miller Institute for Basic Research in Science at UC Berkeley. Part of the research was conducted at the Jet Propulsion Laboratory, California Institute of Technology, under contract with the National Aeronautics and Space Administration (NASA). The Arecibo Observatory is part of the National Astronomy and Ionosphere Center, which is operated by Cornell University under a cooperative agreement with the National Science Foundation and with support from NASA.

REFERENCES

BUTLER, B. J., D. O. MUHLEMAN, AND M. A. SLADE 1993. Mercury: Full-disk radar images and the detection and stability of ice at the north pole. *J. Geophys. Res* **98,** 15,003–15,024.

CAMPBELL, D. B., J. K. HARMON, AND I. I. SHAPIRO 1989. Radar observations of comet Halley. *Astrophys. J.* **338,** 1094–1105.

CAMPBELL, M. J., AND J. ULRICHS 1969. Electrical properties of rocks and their significance for lunar radar observations. *J. Geophys. Res.* **74,** 5867–5881.

CORNWELL, T., AND E. B. FOMALONT 1989. Self-Calibration. In *Synthesis Imaging in Radio Astronomy* (R. A. Perley, F. R. Schwab, A. H. Bridle, Eds.), Vol. 6, pp. 185–198. Astronomic Society of the Pacific Conference Series.

DICKEL, J. R. 1979. Radio observations of asteroids. In *Asteroids* (T. Gehrels, Ed.), pp. 212–221. Univ. of Arizona Press, Tucson.

FOMALONT, E. B. 1993. Paper presented at the XXIV General Assembly of the International Scientific Radio Union, paper JA–7, Kyoto, Japan, Aug. 25 to Sept. 2, 1993.

GARY, B. L., AND S. J. KEIHM 1978. Interpretation of ground-based microwave measurements of the Moon using a detailed regolith properties model. *Proc. Ninth Lunar Sci. Conf., Geochim. Cosmochim. Acta* Vol. 3(Suppl. 9), 2885–2900.

GOLDSTEIN, R. M., R. F. JURGENS, AND Z. SEKANINA 1984. A radar study of comet IRAS–Araki–Alcock 1983d. *Astron. J.* **89,** 1745–1754.

HARMON, J. K., D. B. CAMPBELL, A. A. HINE, I. I. SHAPIRO, AND B. G. MARSDEN 1989. Radar observations of comet IRAS–Araki–Alcock. *Astrophys. J.* **338,** 1071–1093.

MAGNUSSON, P. 1986. Distribution of spin axes and senses of rotation for 20 large asteroids. *Icarus* **68,** 1–39.

MAGNUSSON, P. 1989. Pole determinations of asteroids. In *Asteroids II* (R. P. Binzel, T. Gehrels, and M. S. Matthews, Eds.), pp. 1180–1190. Univ. of Arizona Press, Tucson.

MCKAY, D. S., T. D. SWINDLE, AND R. GREENBERG 1989. Asteroid regoliths: What we do not know. In *Asteroids II* (R. P. Binzel, T. Gehrels, and M. S. Matthews, Eds.), pp. 617–642. Univ. of Arizona Press, Tucson.

MILLIS, R. L., AND D. W. DUNHAM 1989. Precise measurement of asteroid sizes and shapes from occultations. In *Asteroids II* (R. P. Binzel, T. Gehrels, and M. S. Matthews, Eds.), pp. 148–170. Univ. of Arizona Press, Tucson.

MITCHELL, D. L. 1993. *Microwave Imaging of Mercury's Thermal Emission: Observations and Models.* Ph.D. thesis, University of California, Berkeley.

MITCHELL, D. L., AND I. DE PATER 1994. Microwave imaging of Mercury's thermal emission: Observations and models. *Icarus.* **110,** 2–32.

MUHLEMAN, D. O., A. W. GROSSMAN, B. J. BUTLER, AND M. A. SLADE 1990. Radar reflectivity of Titan. *Science* **248,** 975–980.

MUHLEMAN, D. O., A. W. GROSSMAN, B. J. BUTLER, AND M. A. SLADE 1991. Radar images of Mars. *Science* **253,** 1508–1513.

OSTRO, S. J. 1993. Planetary and radar astronomy. *Rev. Mod. Phys.* **65,** 1235–1279.

OSTRO, S. J., D. B. CAMPBELL, AND I. I. SHAPIRO 1985. Mainbelt asteroids: Dual-polarization radar observations. *Science* **229,** 442–446.

OSTRO, S. J., R. CONNELLY, AND L. BELKORA 1988. Asteroid shapes from radar echo spectra: A new theoretical approach. *Icarus* **73,** 15–24.

OSTRO, S. J., D. B. CAMPBELL, J. F. CHANDLER, A. A. HINE, R. S. HUDSON, K. D. ROSEMA, AND I. I. SHAPIRO 1991. Asteroid 1986 DA: Radar evidence for a metallic composition. *Science* **252,** 1399–1404.

OSTRO, S. J., R. F. JURGENS, K.D. ROSEMA, R. WINKLER, D. HOWARD, R. ROSE, M. A. SLADE, D. K. YEOMANS, D. B. CAMPBELL, P. PERILLAT, J. F. CHANDLER, I. I. SHAPIRO, R. S. HUDSON, P. PALMER, AND I. DE PATER 1993. Radar imaging of asteroid 4179 Toutatis. *Bull. Am. Astron. Soc.* **25,** 1126.

SCALTRITI, F., V. ZAPPALA, R. STANZEL, C. BLANCO, S. CATALANO, AND J. W. YOUNG 1980. *Icarus* **43,** 391–398.

SLADE, M. A., B. J. BUTLER, AND D. O. MUHLEMAN 1992. Mercury radar imaging: Evidence for polar ice. *Science* **258,** 635–640.

TEDESCO, E. F. 1989. Asteroid magnitudes, UBV colors, and IRAS

albedos and diameters. In *Asteroids II* (R. P. Binzel, T. Gehrels, and M. S. Matthews, Eds.), pp. 1090–1138. Univ. of Arizona Press, Tucson.

THOMPSON, A. R., MORAN, J. M., SWENSON, G. W., JR. 1986. *Interferometry and Synthesis in Radio Astronomy*. Wiley, New York.

THOLEN, D. J. 1989. Asteroid taxonomic classifications. In *Asteroids II* (R. P. Binzel, T. Gehrels, and M. S. Matthews, Eds.), pp. 1139–1150. Univ. of Arizona Press, Tucson.

TRYKA, K. A., AND D. O. MUHLEMAN 1992. Reflection and emission properties on Venus: Alpha Regio. *J. Geophys. Res.* **97,** 13,379–13,394.

YEOMANS, D. K., S. J. OSTRO, AND P. W. CHODAS 1987. Radar astrometry of near-Earth asteroids. *Astron. J.* **94,** 189–200.